

Article

Facile Synthesis of Porous g-C₃N₄ with Enhanced Visible-Light Photoactivity

Guangyuan Yao ^{1,2}, Yuqiang Liu ², Jingcai Liu ^{2,*} and Ya Xu ^{2,*}

¹ State Key Laboratory of Environmental Criteria and Risk Assessment, Chinese Research Academy of Environmental Sciences, Beijing 100012, China; slxw.yao1990@hotmail.com

² Research Institute of Soil and Solid Waste, Chinese Research Academy of Environmental Sciences, Beijing 100012, China; liuyq@craes.org.cn

* Correspondence: wdf04@163.com (J.L.); xuya@craes.org.cn (Y.X.)

Abstract: Porous graphitic carbon nitride (g-C₃N₄) was prepared by dicyandiamide and urea via the pyrolysis method, which possessed enhanced visible-light-driven photocatalytic performance. Its surface area was increased from 17.12 to 48.00 m²/g. The porous structure not only enhanced the light capture capacity, but also accelerated the mass transfer ability. The Di (Dicyandiamide)/Ur (Urea) composite possessed better photocatalytic activity for Rhodamine B in visible light than that of g-C₃N₄. Moreover, the Di/Ur-4:5 composite showed the best photoactivity, which was almost 5.8 times that of g-C₃N₄. The enhanced photocatalytic activity showed that holes and superoxide radical played a key role in the process of photodegradation, which was ascribed to the enhanced separation of photogenerated carriers. The efficient separation of photogenerated electron-hole pairs may be owing to the higher surface area, O dopant, and pore volumes, which can not only improve the trapping opportunities of charge carriers but also the retarded charge carrier recombination. Therefore, it is expected that the composite would be a promising candidate material for organic pollutant degradation.

Keywords: porous g-C₃N₄; O doping; visible-light irradiation; photocatalysis



Citation: Yao, G.; Liu, Y.; Liu, J.; Xu, Y. Facile Synthesis of Porous g-C₃N₄ with Enhanced Visible-Light Photoactivity. *Molecules* **2022**, *27*, 1754. <https://doi.org/10.3390/molecules27061754>

Academic Editor: Abel Santos

Received: 2 December 2021

Accepted: 10 January 2022

Published: 8 March 2022

Publisher's Note: MDPI stays neutral with regard to jurisdictional claims in published maps and institutional affiliations.



Copyright: © 2022 by the authors. Licensee MDPI, Basel, Switzerland. This article is an open access article distributed under the terms and conditions of the Creative Commons Attribution (CC BY) license (<https://creativecommons.org/licenses/by/4.0/>).

1. Introduction

Nowadays, environmental pollution has become a worldwide problem of high concern, especially in developing countries. Therefore, many technologies have been applied to deal with this issue, such as chemical oxidation and reduction [1,2], adsorption [3,4], coagulation [5], extraction [6,7] and biological treatment [8]. However, these technologies have the disadvantages of secondary pollution and limited application. Therefore, photocatalysts have attracted more and more attention because of their utilization of abundant solar energy, having no need for additional reagents, and no production of waste. The g-C₃N₄ was turned to be a novel organic semiconductor with excellent visible-light response because of its suitable band gap (2.7 eV), stable thermal and chemical properties, and low cost [9]. Generally, both low surface area and separation efficiency of photogenerated electron-hole pairs can depress the photoactivity of g-C₃N₄. Hence, various methods have been carried out to overcome these problems, such as coupling with semiconductors, metal oxide or polymers [10–15], ion doping [16–19], noble metal deposition [20–23], controlling morphology [24–26] and loading on carriers [9,27].

Among these methods, porous g-C₃N₄ has gained increasing attention because of its large surface area with more active sites, which could facilitate mass transfer ability and improve its photocatalytic performance. Generally, porous g-C₃N₄ can be obtained via soft-templating or silica-templating methods. As for the soft-templating methods, the carbon left in the products from the template might restrain its photoactivity. The silica-templating method is another important way to synthesize porous g-C₃N₄. However, it

involves the further removal of silica by hydrogen fluoride, which is hazardous and toxic to the environment. Therefore, it is urgent to synthesize porous $g\text{-C}_3\text{N}_4$ facily and friendly.

Generally, we use dicyandiamide or urea to synthesize $g\text{-C}_3\text{N}_4$. However, the very low yield of porous $g\text{-C}_3\text{N}_4$ from urea may limit its practical application. The bulk $g\text{-C}_3\text{N}_4$ with low surface area could be obtained from dicyandiamide, which greatly depresses its photocatalytic performance. Therefore, we obtain $g\text{-C}_3\text{N}_4$ by dicyandiamide, and use urea as a nontoxic bubble template, which can produce gas bubbles during the heating process and then form a porous structure in the target composites. The porous $g\text{-C}_3\text{N}_4$, synthesized via dicyandiamide and urea as co-precursors, is expected to have enhanced visible-light-driven photocatalytic performance [28].

In the current work, we gained the porous $g\text{-C}_3\text{N}_4$ by dicyandiamide and urea via the pyrolysis method. Then, we characterized the structure, morphology and physicochemical properties of the photocatalysts. Consequently, Rhodamine B was used as the target pollutant to assess its photocatalytic performance. Meanwhile, we studied the photocatalytic activity under visible light with a different mass ratio of dicyandiamide and urea. Furthermore, we also systematically investigated the improved photocatalytic performance, as well as the enhancement mechanism according to the above analysis.

2. Results and Discussion

2.1. XRD Analysis

The XRD patterns of Di/Ur composites and $g\text{-C}_3\text{N}_4$ were displayed in Figure 1. All samples exhibited the typical diffraction peaks at $2\theta = 12.8^\circ$ and 27.6° , which could be attributed to the interlayer stacking of aromatic systems and the in-plane structure motifs, respectively. Furthermore, the Di/Ur composites all possessed higher intensities than that of $g\text{-C}_3\text{N}_4$, and increased as the mass rates of urea and dicyandiamide increased.

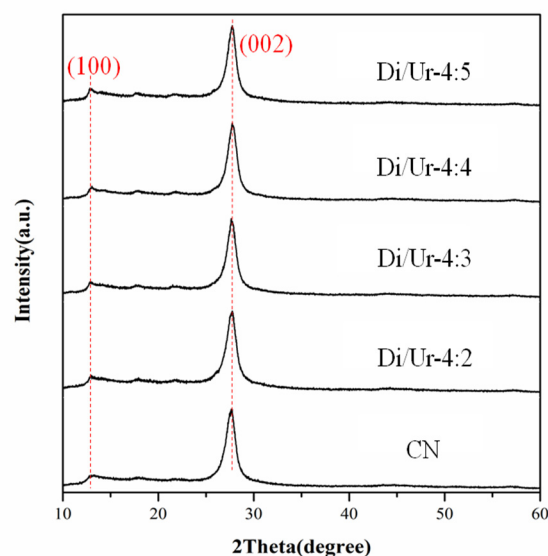


Figure 1. XRD patterns of $g\text{-C}_3\text{N}_4$ and Di/Ur composites.

2.2. SEM Analysis

Figure 2a,b display the morphology and structures of CN and the Di/Ur-4:5 composite, and it can be seen that the CN possessed bulk structure, which was formed by lamellar structures stacking with each other. However, the Di/Ur-4:5 composite possessed a loose structure and pores in its framework, which were beneficial for the photocatalytic performance.

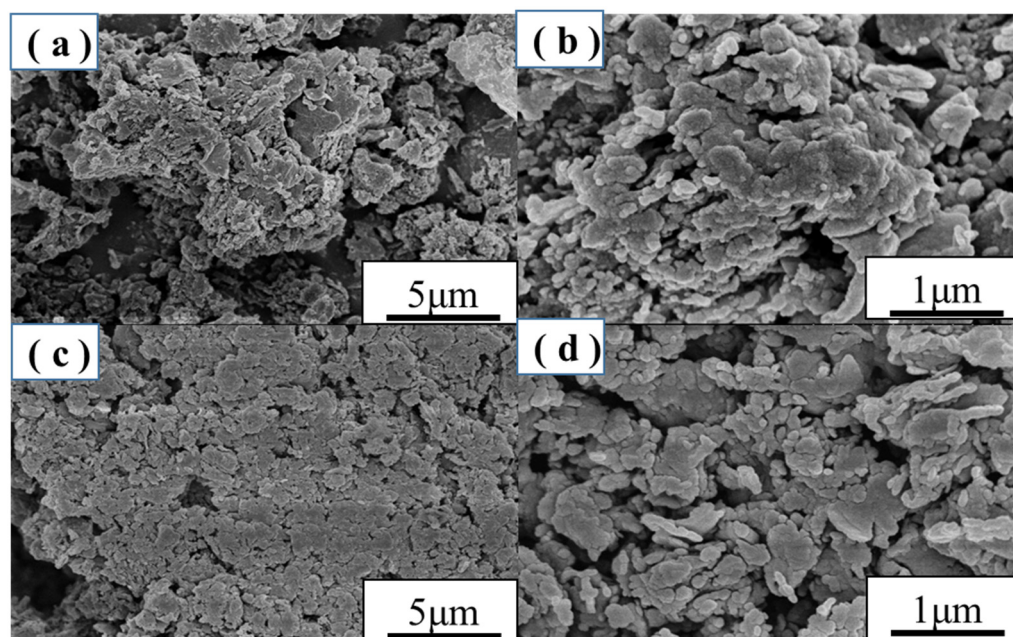


Figure 2. SEM images of (a,b) g-C₃N₄ and (c,d) Di/Ur-4:5 composite.

Furthermore, the N₂ adsorption–desorption isotherms of g-C₃N₄ and Di/Ur composites are shown in Figure 3. The adsorption–desorption isotherms of Di/Ur-4:5 composite exhibited a type IV curve with a small hysteresis loop, revealing the presence of mesoporous structure in the Di/Ur-4:5 composite. Then, the pore structure characterization of g-C₃N₄ and Di/Ur composites was also conducted, and the parameters were presented in Table 1. The as-synthesized Di/Ur samples possessed enhanced surface areas and pore volumes compared with those of CN, improving the adsorption capacity and providing more active sites for the photodegradation of Rh B [29–31].

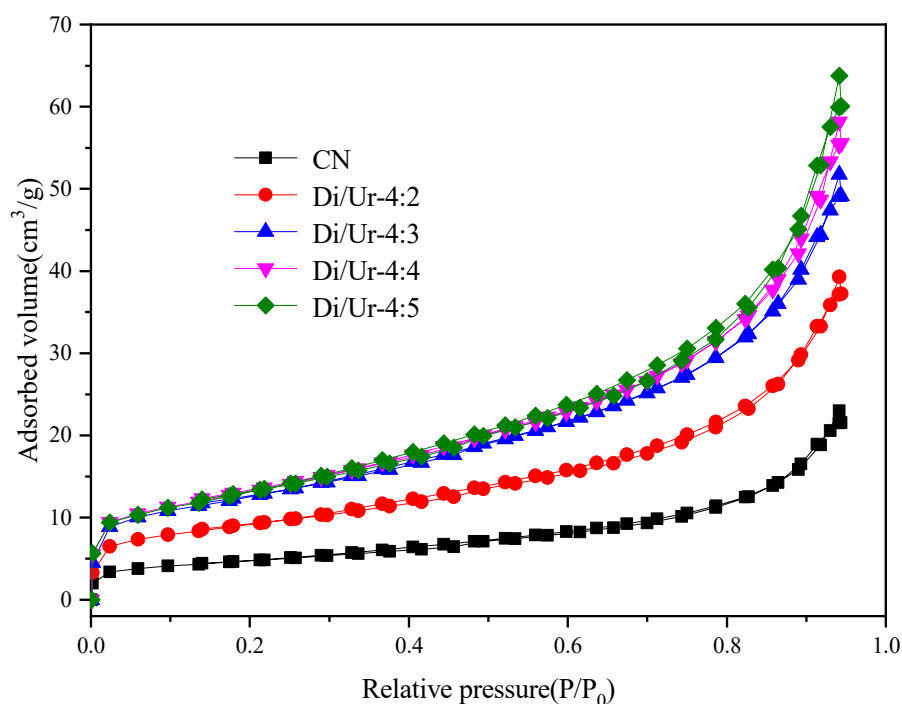


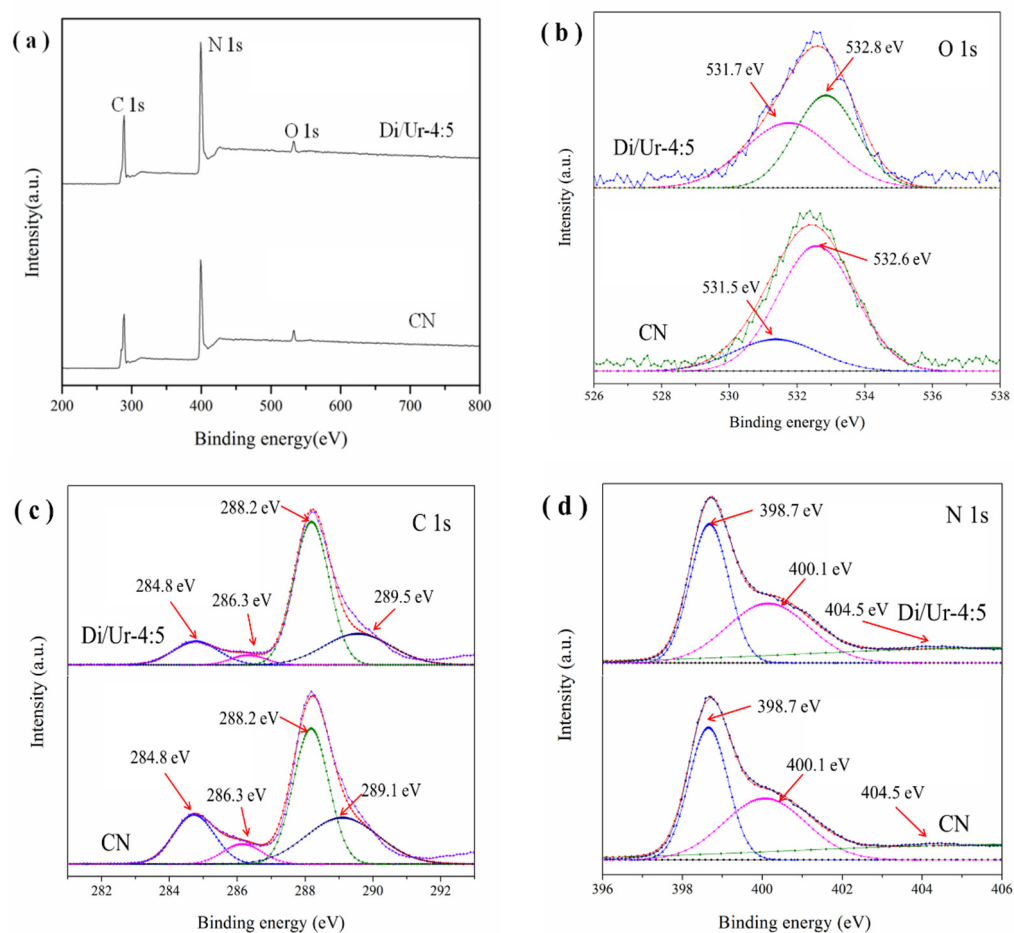
Figure 3. Nitrogen adsorption–desorption isotherms of g-C₃N₄ and the as-prepared Di/Ur composite.

Table 1. BET parameters of $g\text{-C}_3\text{N}_4$ and the obtained Di/Ur samples.

Samples	BET Surface Area (m ² /g)	Pore Volume (cm ³ /g)	Average Pore Diameter (nm)
CN	17.115	0.038	8.315
Di/Ur-4:2	32.483	0.065	7.490
Di/Ur-4:3	44.694	0.085	7.167
Di/Ur-4:4	46.919	0.096	7.675
Di/Ur-4:5	48.002	0.107	8.220

2.3. XPS Analysis

The chemical bonding between the surface elements was determined. It demonstrated that the peaks of N 1s, C 1s and O 1s existed in both the Di/Ur-4:5 sample and $g\text{-C}_3\text{N}_4$. Moreover, the intensity of all spectra in the Di/Ur-4:5 sample was stronger than that of $g\text{-C}_3\text{N}_4$ (Figure 4a). The high-resolution spectra of O1s spectra (Figure 4b) can be divided into two peaks. The peaks at 531.6 and 532.8 eV should be attributed to the formation of the C-O-C species and the surface-adsorbed water, respectively [32]. This result confirmed that O atoms were bonded with C atoms in the basic structure of the photocatalyst. The C 1s spectra (Figure 4c) can be separated into four peaks. The peaks at 284.8, 286.3 and 288.2 eV should arise from the sp^2 C-C bonds, C-NH₂ species, and the sp^2 -hybridized carbon in the N-containing aromatic ring N-C-N, respectively [20]. Moreover, the weak peak at 289.5 eV also confirmed the creation of a C-O bond [33,34]. The N1s spectra (Figure 4d) exhibited peaks at 398.7, 400.1 and 404.5 eV, attributing to the pyridinic nitrogen of C=N-C, bridge N in N-[C]3N3 and π -excitations, respectively [33,35].

**Figure 4.** The XPS of Di/Ur-4:5 and CN for (a) survey spectrum; (b) O 1s; (c) C 1s; (d) N 1s.

2.4. Photocatalytic Performance

The Rh B was used as the target pollutant to examine the photoactivities under visible-light irradiation ($\lambda \geq 420$ nm). The results showed that all the Di/Ur composites exhibited better adsorption performance than $g\text{-C}_3\text{N}_4$ (Figure 5a), and it raised as the mass rate of urea increased. Generally, the adsorption sites on the surface of the sample increased with higher specific surface area and larger pore volumes, which enhanced its adsorption performance. These results corresponded to the BET analysis. Meanwhile, the photocatalytic performance of the Di/Ur composites were greatly enhanced, compared with $g\text{-C}_3\text{N}_4$, and increased as the mass rate of urea raised. Moreover, the Di/Ur-4:5 composite possessed the optimal photoactivities, and the photodegradation rate towards Rh B was almost 100% in 6 h under visible light. Therefore, we can infer that a porous structure with a greater surface area could improve mass transfer ability and photocatalytic performance, due to the more possible photocatalytic reaction sites exposed on its surface [9].

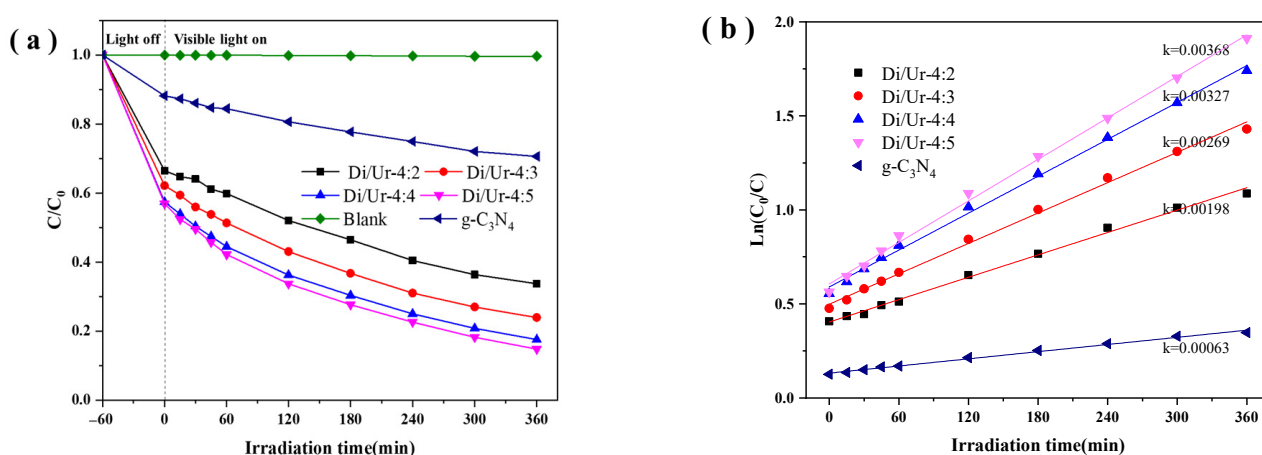


Figure 5. Photocatalytic degradation (a), and linear transform $\ln(C_0/C)$ of the kinetic curves (b), of RhB under visible light.

To get a deep understanding of the photocatalytic process, the kinetic experiments for Rh B photodegradation were conducted, and the results are displayed in Figure 5b. Generally, the pseudo-first order model can best describe the process of photodegradation [36]. The photoactivities of the obtained samples are as follows: Di/Ur-4:5 > Di/Ur-4:4 > Di/Ur-4:3 > Di/Ur-4:2 > $g\text{-C}_3\text{N}_4$. Meanwhile, it is apparent that all the Di/Ur composites possessed higher constants k than that of $g\text{-C}_3\text{N}_4$. The Di/Ur-4:5 sample exhibited the highest reaction rate constant, which was 5.8 times as much as that of $g\text{-C}_3\text{N}_4$. The high reaction rate constant may be attributed to the rising surface area, as depicted in Table 1.

We also investigated the stability and reusability of the Di/Ur-4:5 sample (Figure 6). It can be seen that the Di/Ur-4:5 sample showed excellent reusability during the photocatalytic reaction, and there was no significant deactivation even after four reaction runs. The slight descendant in the fourth run was attributed to intermediate poison on the surface of photocatalysts, which will lower the electron transfer velocity [37].

2.5. Optical Properties

Generally, the optical adsorption properties of the photocatalyst have a great effect on the photocatalytic performance. The UV-vis optical absorption spectra of the Di/Ur composites and $g\text{-C}_3\text{N}_4$ are displayed in Figure 7.

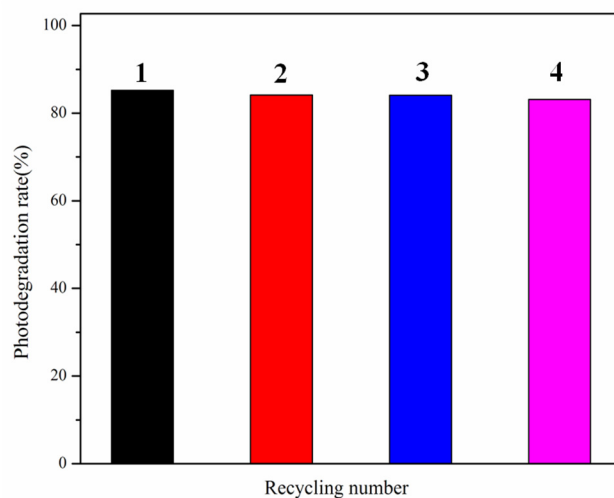


Figure 6. Recycling tests for the photodegradation of RhB over the Di/Ur-4:5 composite under visible light.

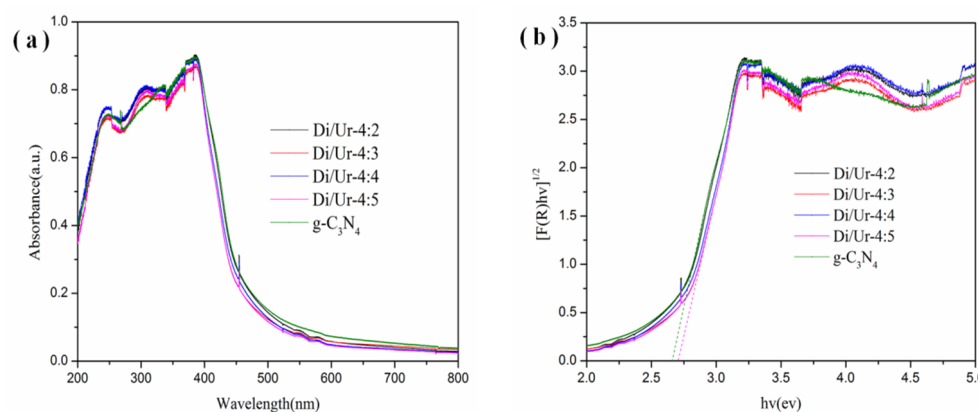


Figure 7. UV-Vis DRS (a), and band gaps (b), of $g\text{-C}_3\text{N}_4$ and the as-prepared Di/Ur composites.

The results showed that the whole samples displayed excellent optical adsorption from UV light to visible light. The adsorption edge was at around 450 nm, and then extended to the region near 600 nm, which can be assigned to its smooth cleavage plane. This indicated that the porous structure may improve the utilization efficiency of visible light and then enhance its photoactivities (Figure 7a). Furthermore, the band gaps of the Di/Ur composites and $g\text{-C}_3\text{N}_4$ are presented in Figure 7b. The band gaps of Di/Ur composites (2.72 eV) were a little larger than that of $g\text{-C}_3\text{N}_4$ (2.67 eV).

To further make clear the behaviors of the photogenerated electron-hole carriers in the photocatalyst, the photoluminescence spectra were recorded. Herein, we present the PL spectrum of the Di/Ur-4:5 composite and $g\text{-C}_3\text{N}_4$. In general, PL intensity determined the recombination efficiency of the photogenerated charge carriers. The lower the PL intensity, the lower the recombination rate. The PL intensity of the Di/Ur-4:5 composite extremely decreased compared with that of $g\text{-C}_3\text{N}_4$ (Figure 8). Moreover, the separation efficiency of the photogenerated electron-hole carriers in the Di/Ur-4:5 composite was significantly accelerated under visible-light irradiation, which was probably attributed to its porous structure and the O dopant. This was consistent with the previous literatures [9,27].

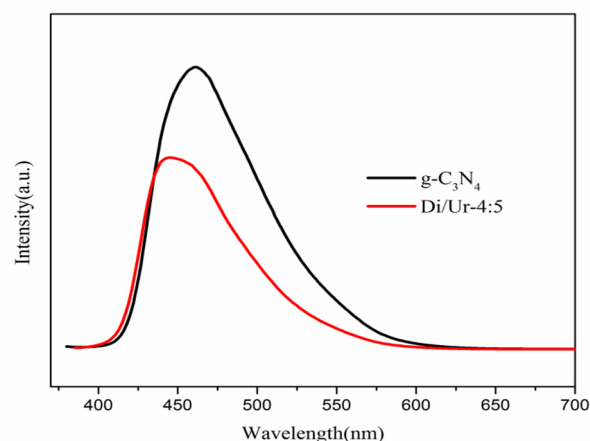


Figure 8. Photoluminescence (PL) spectra of pure $g\text{-C}_3\text{N}_4$ and the Di/Ur-4:5 composite.

Moreover, the transient photocurrent responses and Nyquist impedance plots (EIS) of $g\text{-C}_3\text{N}_4$ and Di/Ur-4:5 composite were also investigated to find out the photogenerated charge separation and electron transfer performance (Figure 9a,b). Notably, the photocurrent sharply declined when the light turned off, and then returned to fixed values when the light turned on. It implied that most photogenerated electrons transferred to the ITO substrates to generate photocurrent under visible-light irradiation. Furthermore, the Di/Ur-4:5 composite showed higher photocurrent intensity than that of $g\text{-C}_3\text{N}_4$, suggesting the higher separation rate of photogenerated charge carriers in the Di/Ur-4:5 composite. Additionally, the photocurrent can reproducibly increase and recover in every on-off cycle of irradiation, demonstrating the high stability in practical applications. Meanwhile, the arc radius of the Di/Ur-4:5 composite was smaller than that of $g\text{-C}_3\text{N}_4$ on the EIS Nyquist plot, which implied that the porous structure changed its charge distribution and made charge transfer easier [28]. The efficient separation of the photogenerated electron-hole pairs may be ascribed to the increased surface area and the enhanced redox potentials, which improved the trapping opportunities of the charge carriers by Rh B and retarded the charge carrier recombination due to the reduced spatial overlap [38]. Meanwhile, the O dopant may modulate the electronic structure and greatly enhance its separation rate [39]. These results are also consistent with our PL analysis.

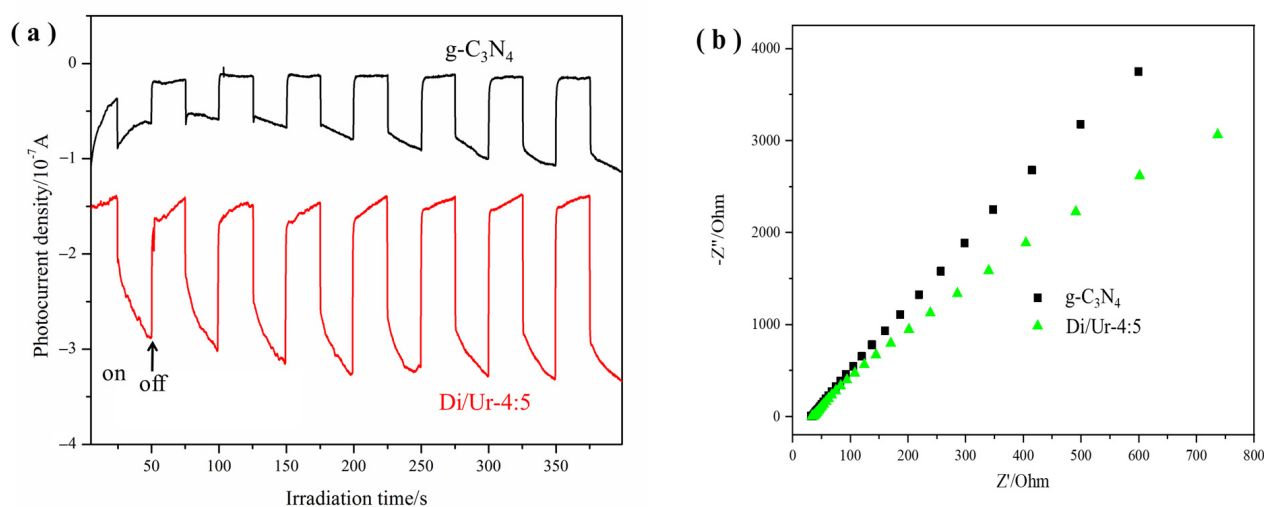


Figure 9. Transient photocurrent responses (a), and EIS Nyquist plots (b), of pure $g\text{-C}_3\text{N}_4$ and Di/Ur-4:5 composite.

2.6. Possible Mechanism

Generally, active species, such as $\bullet\text{O}_2^-$, holes and $\bullet\text{OH}$ radicals, are generated by visible-light irradiation and suspected to be involved in the photocatalytic degradation reaction. To clarify the possible mechanism of the enhanced photoactivity of the Di/Ur-4:5 composite, we used BQ, TBA and EDTA-2Na as scavengers to identify their roles during its photocatalytic process. The photocatalytic degradation rate of Rh B was almost 100% without the addition of the scavengers (Figure 10a). When we added BQ and EDTA-2Na, the photocatalytic performance of Di/Ur-4:5 over Rh B notably declined, which indicated that $\bullet\text{O}_2^-$ and holes play a significant role in the photoactivities. However, when we added TBA, the photocatalytic performance of Rh B slightly depressed, which revealed that $\bullet\text{OH}$ were a minor active species. It was concluded that both $\bullet\text{O}_2^-$ and holes were major active species in the photodegradation of Rh B.

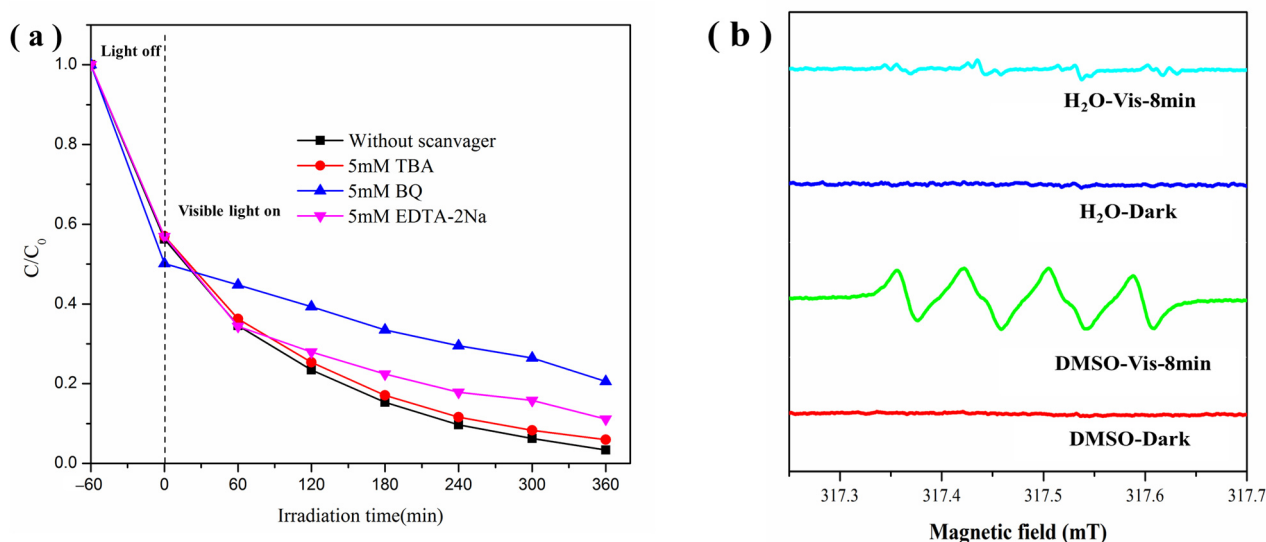


Figure 10. The plots of photogenerated carriers trapping on the photodegradation of RhB under visible light in the presence of the Di/Ur-4:5 composite (a), and ESR spectra of the Di/Ur-4:5 composite in DMSO solvents and water (b), with DMPO.

We also used the ESR technique to determine the active species during the photocatalytic process. It can be seen that there were no ESR signals of $\bullet\text{O}_2^-$ and $\bullet\text{OH}$ species with DMPO in the dark (Figure 10b). Then, a significant evolution of ESR signal in DMSO was observed under visible light, demonstrating the important role of $\bullet\text{O}_2^-$. However, no obvious ESR signal in H_2O were observed, indicating the minor contribution of $\bullet\text{OH}$. These results also corresponded to the radical trapping experiments. Therefore, combined with the above analysis, it was confirmed that both holes and $\bullet\text{O}_2^-$ play a significant role in the photocatalytic process.

Based on the above analysis, the potential electron transfer route and possible mechanism of Di/Ur composites (Figure 11) on the photodegradation of Rh B was proposed. First, the obtained Di/Ur composite can easily absorb visible light because of the porous structure. Second, electrons (e^-) will be transferred from the valence band (VB) to the conduction band (CB), and then create holes (h^+) in the VB. Meanwhile, O dopant, with a higher surface area and larger pore volumes made the photogenerated electron-hole pairs more efficient to migrate, which could retard charge carrier recombination rate due to the reduced spatial overlap, and improve the trapping opportunities of charge carriers by reactants. Then, the adsorbed O_2 could react with e^- to produce enough $\bullet\text{O}_2^-$. Furthermore, the active sites needed for the adsorption and photocatalytic reaction can also be offered by the porous structure. In conclusion, the main active radicals $\bullet\text{O}_2^-$ and the holes generated

in the photocatalyst can effectively decompose the target pollutant (RhB) into ultimate products (CO_2 and H_2O) and other intermediates under visible-light irradiation.

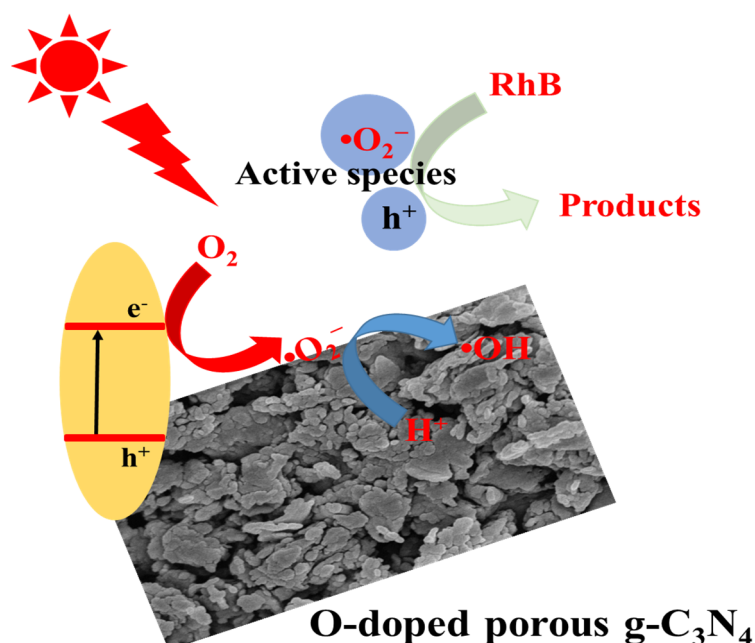


Figure 11. Schematic illustration of the enhanced photocatalytic mechanism of Di/Ur composites under visible-light irradiation.

3. Materials and Methods

3.1. Materials

Dicyandiamide ($\text{C}_2\text{H}_4\text{N}_4$, AR, 98.5%/wt%), rhodamine B ($\text{C}_{28}\text{H}_{31}\text{ClN}_2\text{O}_3$, AR, 98.5%/wt%), urea ($\text{CH}_4\text{N}_2\text{O}$, AR, 99.0%/wt%), edetate disodium (EDTA-2Na, AR, 99.0%/wt%), benzoquinone (BQ, AR, 98.0%/vol%) and tert-butanol (TBA, GR, 99.5%/wt%). Distilled water was used in all the experiments.

3.2. Preparation of Di/Ur Composites

Firstly, we finely grounded the mixture of dicyandiamide and urea via mortar. Secondly, the obtained mixture was annealed for 4 h at 550°C . After cooling down to the room temperature, the yellow powder was finely grounded and then heated at 500°C for 2 h. Then, we collected the final resulting yellow products for further characterization and photocatalytic measurements. Finally, according to the different mass rates of dicyandiamide and urea, we defined the obtained Di/Ur composites as Di/Ur-4:2, Di/Ur-4:3, Di/Ur-4:4 and Di/Ur-4:5, respectively.

Similarly, we gained the $\text{g-C}_3\text{N}_4$ (CN) by dicyandiamide via the pyrolysis method at the same thermal conditions.

3.3. Characterization

X-ray diffraction (XRD) was recorded on a D8 advance X-ray diffractometer (Bruker, Billerica, MA, USA) equipped with Cu-K α radiation ($\lambda = 0.154056\text{ nm}$) to identify the crystalline phase of the obtained photocatalysts. The samples were scanned in the range of 2θ from 10° to 80° with 0.02° step, at a scanning speed of $4^\circ/\text{min}$. An S-4800 scanning electron microscopy (Hitachi, Japan) was applied to investigate the surface morphology of the samples. The surface area of samples was performed by N_2 adsorption at 77 K on a constant volume adsorption apparatus (JW-BK, JWGB Sci. and Tech., Beijing, China) and calculated by the Brunauer–Emmett–Teller (BET) method. The photoluminescence spectra were measured on a Hitachi F-7000 fluorescence spectrophotometer with an excitation wavelength of 400 nm for all the samples. The optical properties of the as-prepared samples

were investigated by UV-vis diffuse reflectance spectroscopy (DRS) using a UV-vis spectrophotometer (U-3010, Hitachi, Toyko, Japan), where BaSO₄ was used as the reference. The band gap values were calculated by extrapolating the linear part of the plot of $(F(R)h\nu)^{1/2}$ versus $h\nu$: $F(R)h\nu = A(h\nu - E_g)^2$, where $F(R) = (1 - R)^2/2R$ stands for the Kubelka–Munk function calculated from the reflectance spectrum, and $h\nu$ is the photon energy expressed in eV. The electron spin resonance (ESR) signals of radical spin trapped by DMPO was at an ambient temperature on a JEOL (FA-200) spectrometer under visible-light irradiation of the suspension (0.05 mg/mL photocatalyst, 100 mM DMPO). The settings for ESR measurements were as follows: center field 324.019 mT, microwave frequency 9053.727 MHz, and power 0.99800 mW. Finally, the photocurrent and electrochemical impedance spectroscopy (EIS) of g-C₃N₄ and Di/Ur-4:5 composite were measured in a 0.1 M Na₂SO₄ aqueous solution with an electrochemical analyzer (CHI-660B, Shanghai, China). X-ray photoelectron spectroscopy (XPS) analysis was performed on the photoelectron spectrometer (Thermo Scientific Escalab 250Xi, Waltham, MA, USA) using monochromatic Al K α radiation energy ($\lambda = 1486.6$ eV). Binding energies for the high-resolution spectra were calibrated by setting C 1 s at 284.8 eV.

3.4. Photoactivity Measurements

We used Rh B as a target pollutant to assess the photocatalytic performance of the as-synthesized samples under a 600 W Xenon lamp with a cut-off filter of 420 nm. First of all, 0.2 g of the photocatalysts was put into 100 mL of Rh B (10 ppm) aqueous solution and then magnetically stirred in the dark for 1 h to reach the adsorption–desorption equilibrium. Sequentially, 3 mL of suspension was collected at a certain time interval and centrifuged to remove photocatalyst particles for further analysis. Finally, the photodegradation effect was identified via a UV-vis spectrophotometer. We also used g-C₃N₄, Di/Ur-4:2, Di/Ur-4:3, Di/Ur-4:4 and Di/Ur-4:5 as references, and conducted comparative experiments under the same conditions. In addition, all the experiments were carried out in triplicates.

4. Conclusions

In summary, the porous g-C₃N₄ was successfully obtained via the pyrolysis method. The SEM, BET and XPS analyses revealed that the prepared samples possessed porous structures and O dopants, which not only enhanced light capture capacity but also accelerated mass transfer ability. The visible-light photoactivities of the obtained Di/Ur composites were greatly enhanced. Moreover, the Di/Ur-4:5 composite possessed the optimal photocatalytic performance towards RhB, which was almost 5.8 times that of g-C₃N₄. Meanwhile, it also exhibited exceptional stability and reusability. It was indicated that $\bullet\text{O}_2^-$ and holes were the major active species, and the excellent photocatalytic performance in visible light was attributed to the enhanced separation of photogenerated carriers. The efficient separation rates may be ascribed to the O dopant and the improved pore structure, which improved the trapping opportunities of charge carriers by RhB and retarded the charge carrier recombination. Therefore, this study not only shed light on the facile construction of porous g-C₃N₄, but also showed great potential in the fields of the organic pollutant degradation.

Author Contributions: G.Y.: Conceptualization; funding acquisition; investigation; methodology; resources; writing—review and editing. Y.L.: funding acquisition; supervision; resources. J.L.: Investigation; methodology; supervision; resources. Y.X.: investigation; methodology; writing—review and editing. All authors have read and agreed to the published version of the manuscript.

Funding: This research was financially supported by the National Key Research and Development Plan (2018YFC1800902) and the China Scholarship Council (CSC).

Institutional Review Board Statement: Not applicable.

Informed Consent Statement: Not applicable.

Data Availability Statement: Not applicable.

Acknowledgments: Not applicable.

Conflicts of Interest: The authors declare no conflict of interest.

Sample Availability: Samples of g-C₃N₄ and Di/Ur composites are available from the authors.

References

1. Rayaroth, M.P.; Oh, D.; Lee, C.S.; Kang, Y.G.; Chang, Y.S. In situ chemical oxidation of contaminated groundwater using a sulfidized nanoscale zerovalent iron-persulfate system: Insights from a box-type study. *Chemosphere* **2020**, *257*, 127117. [[CrossRef](#)] [[PubMed](#)]
2. Khalil, A.; Ali, N.; Khan, A.; Asiri, A.M.; Kamal, T. Catalytic potential of cobalt oxide and agar nanocomposite hydrogel for the chemical reduction of organic pollutants. *Int. J. Biol. Macromol.* **2020**, *164*, 2922–2930. [[CrossRef](#)] [[PubMed](#)]
3. Sun, Z.; Yao, G.; Liu, M.; Zheng, S. In situ synthesis of magnetic MnFe₂O₄/diatomite nanocomposite adsorbent and its efficient removal of cationic dyes. *J. Taiwan Inst. Chem. Eng.* **2017**, *71*, 501–509. [[CrossRef](#)]
4. Cao, H.; Wu, X.; Syed-Hassan, S.S.A.; Zhang, S.; Mood, S.H.; Milan, Y.J.; Garcia-Perez, M. Characteristics and mechanisms of phosphorous adsorption by rape straw-derived biochar functionalized with calcium from eggshell. *Bioresour. Technol.* **2020**, *318*, 124063. [[CrossRef](#)] [[PubMed](#)]
5. Wang, J.; Tang, X.; Xu, Y.; Cheng, X.; Li, G.; Liang, H. Hybrid UF/NF process treating secondary effluent of wastewater treatment plants for potable water reuse: Adsorption vs. coagulation for removal improvements and membrane fouling alleviation. *Environ. Res.* **2020**, *188*, 109833. [[CrossRef](#)] [[PubMed](#)]
6. Yu, X.; Cui, J.; Liu, C.; Yuan, F.; Guo, Y.; Deng, T. Separation of magnesium from high Mg/Li ratio brine by extraction with an organic system containing ionic liquid. *Chem. Eng. Sci.* **2021**, *229*, 116019. [[CrossRef](#)]
7. Zhang, L.; Lv, P.; He, Y.; Li, S.; Chen, K.; Yin, S. Purification of chlorine-containing wastewater using solvent extraction. *J. Clean. Prod.* **2020**, *273*, 122863. [[CrossRef](#)]
8. Chambi-Rocha, A.; Cabrera-Dominguez, M.E.; Dominguez-Reyes, A. Breathing mode influence on craniofacial development and head posture. *J. Pediatr. (Rio J.)* **2018**, *94*, 123–130. [[CrossRef](#)]
9. Yao, G.; Sun, Z.; Zheng, S. Synthesis and enhanced visible-light photocatalytic activity of wollastonite/g-C₃N₄ composite. *Mater. Res. Bull.* **2017**, *86*, 186–193. [[CrossRef](#)]
10. Sun, J.X.; Yuan, Y.P.; Qiu, L.G.; Jiang, X.; Xie, A.J.; Shen, Y.H.; Zhu, J.F. Fabrication of composite photocatalyst g-C₃N₄-ZnO and enhancement of photocatalytic activity under visible light. *Dalton Trans.* **2012**, *41*, 6756–6763. [[CrossRef](#)]
11. Wang, D.; Sun, H.; Luo, Q.; Yang, X.; Yin, R. An efficient visible-light photocatalyst prepared from g-C₃N₄ and polyvinyl chloride. *Appl. Catal. B Environ.* **2014**, *156–157*, 323–330. [[CrossRef](#)]
12. Li, F.T.; Zhao, Y.; Wang, Q.; Wang, X.J.; Hao, Y.J.; Liu, R.H.; Zhao, D. Enhanced visible-light photocatalytic activity of active Al₂O₃/g-C₃N₄ heterojunctions synthesized via surface hydroxyl modification. *J. Hazard. Mater.* **2015**, *283*, 371–381. [[CrossRef](#)]
13. Yao, Y.; Lu, F.; Zhu, Y.; Wei, F.; Liu, X.; Lian, C.; Wang, S. Magnetic core-shell CuFe₂O₄@C₃N₄ hybrids for visible light photocatalysis of Orange II. *J. Hazard. Mater.* **2015**, *297*, 224–233. [[CrossRef](#)]
14. He, J.; Sun, H.; Indrawirawan, S.; Duan, X.; Tade, M.O.; Wang, S. Novel polyoxometalate@g-C₃N₄ hybrid photocatalysts for degradation of dyes and phenolics. *J. Colloid Interface Sci.* **2015**, *456*, 15–21. [[CrossRef](#)]
15. Zhang, R.; Ran, T.; Cao, Y.; Ye, L.; Dong, F.; Zhang, Q.; Yuan, L.; Zhou, Y. Oxygen activation of noble-metal-free g-C₃N₄/α-Ni(OH)₂ to control the toxic byproduct of photocatalytic nitric oxide removal. *Chem. Eng. J.* **2020**, *382*, 123029. [[CrossRef](#)]
16. Cao, L.; Wang, R.; Wang, D. Synthesis and characterization of sulfur self-doped g-C₃N₄ with efficient visible-light photocatalytic activity. *Mater. Lett.* **2015**, *149*, 50–53. [[CrossRef](#)]
17. Gao, J.; Wang, J.; Qian, X.; Dong, Y.; Xu, H.; Song, R.; Yan, C.; Zhu, H.; Zhong, Q.; Qian, G.; et al. One-pot synthesis of copper-doped graphitic carbon nitride nanosheet by heating Cu–melamine supramolecular network and its enhanced visible-light-driven photocatalysis. *J. Solid State Chem.* **2015**, *228*, 60–64. [[CrossRef](#)]
18. Hu, S.; Ma, L.; You, J.; Li, F.; Fan, Z.; Lu, G.; Liu, D.; Gui, J. Enhanced visible light photocatalytic performance of g-C₃N₄ photocatalysts co-doped with iron and phosphorus. *Appl. Surf. Sci.* **2014**, *311*, 164–171. [[CrossRef](#)]
19. Cui, J.; Liang, S.; Wang, X.; Zhang, J. First principle modeling of oxygen-doped monolayer graphitic carbon nitride. *Mater. Chem. Phys.* **2015**, *161*, 194–200. [[CrossRef](#)]
20. Yang, Y.; Guo, Y.; Liu, F.; Yuan, X.; Guo, Y.; Zhang, S.; Guo, W.; Huo, M. Preparation and enhanced visible-light photocatalytic activity of silver deposited graphitic carbon nitride plasmonic photocatalyst. *Appl. Catal. B Environ.* **2013**, *142–143*, 828–837. [[CrossRef](#)]
21. Han, T.; Li, X.; Li, Y.; Cao, W.; Wu, D.; Du, B.; Wei, Q. Gold nanoparticles enhanced electrochemiluminescence of graphite-like carbon nitride for the detection of Nuclear Matrix Protein 22. *Sens. Actuators B Chem.* **2014**, *205*, 176–183. [[CrossRef](#)]
22. Cao, S.-W.; Yuan, Y.-P.; Barber, J.; Loo, S.C.J.; Xue, C. Noble-metal-free g-C₃N₄/Ni(dmgh)₂ composite for efficient photocatalytic hydrogen evolution under visible light irradiation. *Appl. Surf. Sci.* **2014**, *319*, 344–349. [[CrossRef](#)]
23. Jin, C.; Kang, J.; Li, Z.; Wang, M.; Wu, Z.; Xie, Y. Enhanced visible light photocatalytic degradation of tetracycline by MoS₂/Ag/g-C₃N₄ Z-scheme composites with peroxydisulfate. *Appl. Surf. Sci.* **2020**, *514*, 146076. [[CrossRef](#)]
24. Niu, P.; Zhang, L.; Liu, G.; Cheng, H.-M. Graphene-Like Carbon Nitride Nanosheets for Improved Photocatalytic Activities. *Adv. Funct. Mater.* **2012**, *22*, 4763–4770. [[CrossRef](#)]

25. Cai, Q.; Shen, J.; Feng, Y.; Shen, Q.; Yang, H. Template-free preparation and characterization of nanoporous g-C₃N₄ with enhanced visible photocatalytic activity. *J. Alloys Compd.* **2015**, *628*, 372–378. [[CrossRef](#)]
26. Gu, Q.; Liao, Y.; Yin, L.; Long, J.; Wang, X.; Xue, C. Template-free synthesis of porous graphitic carbon nitride microspheres for enhanced photocatalytic hydrogen generation with high stability. *Appl. Catal. B Environ.* **2015**, *165*, 503–510. [[CrossRef](#)]
27. Sun, Z.; Yao, G.; Zhang, X.; Zheng, S.; Frost, R.L. Enhanced visible-light photocatalytic activity of kaolinite/g-C₃N₄ composite synthesized via mechanochemical treatment. *Appl. Clay Sci.* **2016**, *129*, 7–14. [[CrossRef](#)]
28. Zhang, M.; Xu, J.; Zong, R.; Zhu, Y. Enhancement of visible light photocatalytic activities via porous structure of g-C₃N₄. *Appl. Catal. B Environ.* **2014**, *147*, 229–235. [[CrossRef](#)]
29. Li, Y.; Sun, Y.; Dong, F.; Ho, W.K. Enhancing the photocatalytic activity of bulk g-C₃N₄ by introducing mesoporous structure and hybridizing with graphene. *J. Colloid Interface Sci.* **2014**, *436*, 29–36. [[CrossRef](#)]
30. Zhang, S.; Zhao, L.; Zeng, M.; Li, J.; Xu, J.; Wang, X. Hierarchical nanocomposites of polyaniline nanorods arrays on graphitic carbon nitride sheets with synergistic effect for photocatalysis. *Catal. Today* **2014**, *224*, 114–121. [[CrossRef](#)]
31. Zang, Y.; Li, L.; Li, X.; Lin, R.; Li, G. Synergistic collaboration of g-C₃N₄/SnO₂ composites for enhanced visible-light photocatalytic activity. *Chem. Eng. J.* **2014**, *246*, 277–286. [[CrossRef](#)]
32. Mei, R.; Ma, L.; An, L.; Wang, F.; Xi, J.; Sun, H.; Luo, Z.; Wu, Q. Layered Spongy-like O-Doped g-C₃N₄: An Efficient Non-Metal Oxygen Reduction Catalyst for Alkaline Fuel Cells. *J. Electrochem. Soc.* **2017**, *164*, F354–F363. [[CrossRef](#)]
33. Wang, Y.; Wang, H.; Chen, F.; Cao, F.; Zhao, X.; Meng, S.; Cui, Y. Facile synthesis of oxygen doped carbon nitride hollow microsphere for photocatalysis. *Appl. Catal. B Environ.* **2017**, *206*, 417–425. [[CrossRef](#)]
34. Fu, J.; Zhu, B.; Jiang, C.; Cheng, B.; You, W.; Yu, J. Hierarchical Porous O-Doped g-C₃N₄ with Enhanced Photocatalytic CO₂ Reduction Activity. *Small* **2017**, *13*, 1603938. [[CrossRef](#)]
35. Fang, W.; Liu, J.; Yu, L.; Jiang, Z.; Shangguan, W. Novel (Na, O) co-doped g-C₃N₄ with simultaneously enhanced absorption and narrowed bandgap for highly efficient hydrogen evolution. *Appl. Catal. B Environ.* **2017**, *209*, 631–636. [[CrossRef](#)]
36. Wang, B.; de Godoi, F.C.; Sun, Z.; Zeng, Q.; Zheng, S.; Frost, R.L. Synthesis, characterization and activity of an immobilized photocatalyst: Natural porous diatomite supported titania nanoparticles. *J. Colloid Interface Sci.* **2015**, *438*, 204–211. [[CrossRef](#)]
37. Liu, S.; Sun, H.; Suvorova, A.; Wang, S. One-pot hydrothermal synthesis of ZnO-reduced graphene oxide composites using Zn powders for enhanced photocatalysis. *Chem. Eng. J.* **2013**, *229*, 533–539. [[CrossRef](#)]
38. Shen, B.; Hong, Z.; Chen, Y.; Lin, B.; Gao, B. Template-free synthesis of a novel porous g-C₃N₄ with 3D hierarchical structure for enhanced photocatalytic H₂ evolution. *Mater. Lett.* **2014**, *118*, 208–211. [[CrossRef](#)]
39. Zeng, Y.; Liu, X.; Liu, C.; Wang, L.; Xia, Y.; Zhang, S.; Luo, S.; Pei, Y. Scalable one-step production of porous oxygen-doped g-C₃N₄ nanorods with effective electron separation for excellent visible-light photocatalytic activity. *Appl. Catal. B Environ.* **2018**, *224*, 1–9. [[CrossRef](#)]